Fabrication and Preliminary Testing of Silver Patterned Cathodes for Proton Conducting

**IT-SOFC** 

Md Shariful Islam Sozal a, Wenhao Li a, Suprabha Das a, Borzooye Jafarizadeh a, Azmal Huda

Chowdhury a, Chunlei Wang b, Zhe Cheng a\*

<sup>a</sup> Department of Mechanical and Materials Engineering, Florida International University, Miami,

FL, 33174, USA

<sup>b</sup> Department of Mechanical and Aerospace Engineering, University of Miami, Miami, FL, 33146,

**USA** 

\*Correspondence: Dr. Zhe Cheng zhcheng@fiu.edu

**Abstract** 

Dense silver (Ag) cathodes with a defined triple phase boundary (TPB between the interface of

electrolyte, electrode, and gas) length (L<sub>TPB</sub>) and electrode area (A<sub>ELT</sub>) were fabricated by

photolithography and E-beam evaporation over a proton conductive  $BaZr_{0.4}Ce_{0.4}Y_{0.1}Yb_{0.1}O_{3-\delta}$ 

(BZCYYb4411) electrolyte. A bi-layer lift-off resist method appears more versatile than single

layer for successful patterned cathode fabrication. The electrochemical behaviors of the Ag

patterned cathodes over the BZCYYb4411 electrolyte were tested for electrochemical impedance

(EIS) at different temperatures in atmospheres with different concentrations of O<sub>2</sub> and H<sub>2</sub>O. The

results were processed using Distribution of Relaxation Times (DRT) and reaction order analyses

and also fitted to equivalent circuits. The directions of future work on patterned electrodes with

different L<sub>TPB</sub> and A<sub>ELT</sub> and theoretical calculations to gain further insights into the kinetics &

mechanism of cathode oxygen reduction reaction (ORR) over proton conducting electrolyte are

pointed out.

1

Keywords: Proton Conducting SOFC; Photolithography; Silver Patterned Cathodes;

Electrochemical Behavior; O<sub>2</sub>; H<sub>2</sub>O

#### Introduction

Solid oxide fuel cell (SOFC) has been extensively researched for a variety of applications including portable or stationary power generation and transportation<sup>1–5</sup>. The commercialization of conventional SOFCs faces a notable obstacle due to the required high operating temperature - typically ~700-1000°C. The high operating temperature results in prolonged start-up time and difficulties in ensuring compatibility and durability of the materials used in the system, leading to higher than ideal degradation rate<sup>5,6</sup>. To address this challenge, extensive research is currently being conducted on intermediate temperature (400-600°C) solid oxide fuel cell (IT-SOFC), especially *proton conducting* (PC) IT SOFC due to proton conducting ceramic (PCC) electrolytes' high ionic conductivity at intermediate temperature <sup>7–11</sup>.

However, when the operating temperature drops, the oxygen reduction reaction (ORR) at the cathode becomes more critical to the efficient functioning of SOFCs. This is due to sluggish ORR kinetics at intermediate temperatures. The cathode reaction process for oxygen ion conducting SOFC and proton conducting SOFC follows different pathways. The cathode ORR process for conventional SOFC based on oxygen ion (i.e.,  $O^{2-}$  or  $V_O^{\bullet\bullet}$ ) conducting electrolytes would proceed via the pathway of oxygen vacancy

$$O_2 + 4e' + 2V_0^{\bullet \bullet} \leftrightarrow 2O_0^{\times}$$
 (1)

<sup>12,13</sup>. The ORR for oxygen ion conducting SOFCs include elementary steps such as oxygen adsorption, oxygen dissociation, charge transfer, mass transfer of oxide ions into the bulk of the electrolyte<sup>12,13</sup>. The mechanism for ORR via the oxygen vacancy pathway has been extensively

studied using various approaches, including the use of cells with patterned electrodes over oxygen ion conducting electrolytes. In comparison, the cathode ORR process for proton conducting SOFC would proceed via a different pathway, as described below

$$O_2 + 4e' + 4(OH)_O \leftrightarrow 4O_O \times + 2H_2O$$
 (2)

 $^{12,13}$ , that involves proton (or protonated oxygen,  $(OH)_{O}$ ) and water. The ORR for proton conducting SOFC involve even more elementary steps including oxygen adsorption, oxygen dissociation, surface diffusion, charge transfer, mass transfer of proton into the bulk of the electrolyte, as well as water formation and desorption  $^{12-15}$ . Previous studies by He et al., did analysis of the reaction order for the ORR of proton conducting SOFC (i.e., dependence of reaction rate on atmosphere such as  $pO_2$  and  $pH_2O$ ) by hypothesizing eight elemental steps  $^{14}$ , while the study by Grimaud et al. assumed 6 elemental steps  $^{15}$ . However, despite numerous studies, there are still aspects of the ORR mechanism for proton conducting SOFC that remain uncertain.

On the other hand, a classical approach for understanding electrode reactions including ORR was offered by dense patterned electrodes as mentioned <sup>16–29</sup>. The utilization of patterned electrodes enables precise control of both the *length* of the triple phase boundary (TPB) and the *area* of the electrode, linking electrode geometry with reaction kinetics. Significant research has been carried out on electrode reaction mechanism in conventional oxygen ion conducting SOFC utilizing patterned electrodes made of noble metals such as platinum (Pt) or silver (Ag) <sup>16,19–21,23,26–28</sup>. Previous studies showed that for Pt, ORR kinetics is correlated with the length of the TPB <sup>20,23,27,28</sup>. In contrast, Ag is less expensive and has higher electronic conductivity than Pt. One study showed that an SOFC with patterned Ag cathode exhibited comparable performance to Pt cathode with an identical design<sup>21</sup>. Another study showed that the rate-limiting step of the Ag cathode reaction for oxygen ion conducting SOFCs is the bulk diffusion through the Ag electrode at 700-

900°C<sup>16</sup>. Subsequent study reported that at 350-550°C, dissociative oxygen adsorption/reduction might be the rate limiting steps of the Ag cathode reaction for oxygen ion conducting SOFC<sup>30</sup>.

However, for proton conducting IT-SOFC, despite its recent development, there is *no* study carried out utilizing the patterned electrode approach except Haile et al.<sup>31</sup> who used PrBa<sub>0.5</sub>Sr<sub>0.5</sub>Co<sub>1.5</sub>Fe<sub>0.5</sub>O<sub>5+δ</sub>, PBSCF mixed conducting cathode. It is expected that a simpler Ag patterned electrode over a proton conducting electrolyte would be very valuable to help identify the reaction site (i.e., at TPB or cathode surface) and clarify if the proton conducting ceramic electrolyte plays any electro-catalytic role in the ORR reaction. Therefore, this study aims to fabricate Ag patterned cathode on a proton conductive BaZr<sub>0.4</sub>Ce<sub>0.4</sub>Y<sub>0.1</sub>Yb<sub>0.1</sub>O<sub>3-δ</sub> (BZCYYb4411) electrolyte. Preliminary testing for the patterned electrode cells has been carried out showing the effects of moisture (H<sub>2</sub>O) and oxygen (O<sub>2</sub>) concentration on measured electrochemical behaviors. The implications of the preliminary study and the directions for subsequent research have also been discussed.

# **Experimental**

#### Powder synthesis, sintering, and polishing

In this study, BZCYYb4411 proton conducting ceramic electrolyte and PrNi<sub>0.5</sub>Co<sub>0.5</sub>O<sub>3-δ</sub> (PNC, as the counter electrode) powders were synthesized using the Pechini method<sup>32</sup>, and the details have been described previously<sup>32</sup>. To fabricate the proton conducting electrolyte pellet, 0.4 g of BZCYYb4411 powder containing 0.5 wt.% NiO as a sintering aid was pressed using a 13 mm die with a pressure of ~300 MPa. The green pellet was sintered at 1550°C for 10 h in air under a *protective* condition, as previously described<sup>32</sup>. Subsequently, BZCYYb4411 pellets were

subjected to grinding on both surfaces using silicon carbide abrasive papers of varying grit number from 600 to 1200. Finally, the samples underwent a polishing procedure using diamond suspensions of 1, 0.1, and 0.05  $\mu$ m in succession. The thickness of the polished BZCYYb4411 pellet is ~0.5 mm.

# Photolithography for fabrication of Ag patterned electrodes

Photolithography is a microfabrication technique that uses a photomask to transfer a predefined pattern onto a substrate surface through a series of steps. It is widely used in integrated circuit (IC) and sensor fabrication. In the past two decades, photolithography was also used in the fabrication of patterned electrodes for oxygen ion-conducting SOFCs<sup>16,18,19,22–25,27–29,33–36</sup>. However, most previous studies did not provide adequate details on the fabrication process, making reproducing and further fine-tuning of the patterned electrode difficult. Meanwhile, as stated, there have been no studies on the fabrication of patterned electrodes over proton conducting electrolyte except by Haile et al<sup>31</sup>. Therefore, a comprehensive description of the techniques and procedures used in the fabrication of patterned Ag electrodes over BZCYYb4411 electrolyte is given below in detail.

First, a blank photomask was purchased from Nano film and it consists of three layers: a top surface layer of positive photoresist, followed by a layer of chromium and a glass substrate, which is transparent to UV light. The desired pattern for the mask was designed using the Layout Editor software (Free version, 20230301) and subsequently transferred onto the mask by exposing the photoresist layer using a laser mask writer (uPG101, wave length of 405 nm), as illustrated in Fig. 1(a). The laser power used for exposure was 4.8 mW. Following the exposure, the mask was developed using a developer solution (AZ400K (15% Potassium borate/85% water): Water = 1:

4 by volume) to remove the laser-exposed positive photoresist, which resulted in openings in the photoresist layer exposing the chrome layer according to the designed pattern. The exposed chromium was subsequently etched away by immerging the mask in Chromium Etch 1020 AC (containing nitric acid, ceric ammonium nitrate, water; exact concentration unknown due to commercial product) for 3 min, transferring the pattern onto the glass. Finally, the remaining photoresist was removed through reactive ion etching by oxygen plasma, thus completing the fabrication of the mask as shown in Fig. 1.

After the photomask is patterned, the subsequent step involves transferring the pattern onto the substrate coated with a photoresist layer. The photoresist comes in two forms, positive or negative. Positive photoresist, upon UV light exposure, undergoes molecular chain breakage and becomes more soluble in the developer solution<sup>35,37</sup>. As a result, after development, the regions exposed to UV light undergo material removal/dissolution, leaving the unexposed regions intact and insoluble to the developer solution. In comparison, negative photoresist, upon UV light exposure, experiences polymerization and becomes insoluble to the developer solution. Thus, after development, the regions exposed to UV light remain on the substrate<sup>35,37</sup>. Due to the disparity in light dosage between the top and bottom layers, with the top layer experiencing a higher dose, positive photoresists tend to produce overcut profile (i.e., the opening at the photoresist top surface is *wider* than at the bottom or near the substrate), while negative photoresists tend to produce undercut profile (i.e., the opening at the photoresist top surface is *narrower* than at the bottom or near the substrate) and (b).

Because of the difference in sidewall profile, the lift-off process (i.e., the removal of residual photoresist after metal deposition) is easier when using negative photoresist than positive photoresist, as negative photoresist prevents metal from accumulating on the walls of the resist

after deposition<sup>39</sup>. However, negative photoresist often has lower resolution compared to positive photoresist. This is because for negative photoresist, the developer solution tends to infiltrate both the UV-exposed and unexposed areas, which results in reduced resolution or pattern distortion <sup>40–42</sup>. On the contrary, positive photoresist is capable of maintaining its high-resolution pattern unless it is overdeveloped (by being left in the developer solution longer than necessary). Therefore, in this study, positive photoresist was chosen.

To achieve effective lift-off in photolithography with positive photoresist, the use of a *bilayer* resist system composed of a bottom sacrificial layer and a top imaging photoresist layer was found to be crucial in this study<sup>35,43</sup>. Although the sacrificial layer lacks photo-reactivity, it creates undercut during development due to its *higher* dissolution rate than the top imaging photoresist layer. This enables the successful removal of the resists after Ag electrode deposition, as demonstrated in Fig. 2(c). Without this bilayer approach, the lift-off process is challenging due to accumulation of metal on the walls of the resist after deposition. Therefore, in this study, Ag patterned electrodes were fabricated over BZCYYb4411 electrolyte substrates using photolithography with a bilayer resist system.

Prior to the photolithography process, polished BZCYYb4411 substrates underwent cleaning with IPA, acetone, and DI water, followed by a dehydration bake at 170°C for 10 min to improve the adhesion of the resist with the substrate. LOR 3B, as a sacrificial layer, was spin-coated onto the cleaned substrates using the following parameters: 500 rpm for 10 s, 1000 rpm for 10 s, 1500 rpm for 10 s, 2000 rpm for 120 s. Subsequently, the sacrificial layer underwent a soft bake process at 141°C for 90 s to eliminate the solvent in it and improve its adhesion to the substrate. Then, AZ1518, a positive photoresist, was spin-coated over the LOR 3B sacrificial layer on the BZCYYb4411 substrate, using the same spinning parameters. Afterward, the photoresist

underwent a soft bake process at 110°C for 90 s to eliminate solvents and improve adhesion to the sacrificial layer. Subsequently, the substrates were exposed to UV light of 150 mJ/cm<sup>2</sup> to form the pattern. The photoresist was developed in AZ400K developer solution to form the pattern in the photoresist layer (as well as the bottom sacrificial layer, with undercut) over the electrolyte (see

Fig. 3 for photos), which was necessary for subsequent Ag electrode deposition.

In microfabrication, metals are deposited commonly by two techniques: E-beam evaporation and sputtering. For E-beam evaporation, metal deposition is unidirectional as the mean free path of metal atoms is longer than the distance between the substrate and the target due to high vacuum (~10<sup>-7</sup> Torr)<sup>35,37,39</sup>. This results in minimal sidewall deposition and effective lift-off. For sputtering, the lower vacuum (~10-3 Torr) causes a shorter mean free path, leading to non-unidirectional deposition with more sidewall coverage and challenges with lift-off <sup>35,37,39</sup>. In this study, ~75 nm thick Ag layer was deposited onto the BZCYYb4411 substrates by E-beam evaporation (base pressure: 5×10<sup>-6</sup> Torr; soak-1 power: 12%, rise-1 time: 5 min, soak-1 time: 30 s; soak-2 power: 14%, rise-2 time: 10 s, soak-2 time: 30 s). Finally, the lift-off of the remaining photoresist was carried out using Remover PG (N-Methyl Pyrrolidinone) at ~70°C. Microstructural analysis and the EDS line scan of the Ag patterned electrodes over BZCYYb441 electrolyte substrate were done by a scanning electron microscope (SEM JEOL JSM-F100) equipped with energy dispersive Xray spectroscopy (EDS).

# Electrochemical cell fabrication and test

In this study, electrochemical cells with patterned Ag working electrode were fabricated using PNC as the counter electrode. To fabricate cells, at first fritless Ag paste was first brush painted on the contact pad of Ag patterned electrode over BZCYYb4411 electrolyte and dried. PNC slurry

was then brushed onto the opposite side of the electrolyte, as previously discussed, to form the PNC counter electrode, followed by the application of Ag paste over the PNC electrode for current collection  $^{32}$ . The cell then underwent a heat treatment at 600°C for 2 h in simulated air (Ultra Zero Grade, Airgas, <5 ppm  $H_2O$  and  $CO_2$  by volume).

Following the heat treatment at 600°C for 2 h, electrochemical impedance spectroscopy (EIS) tests were conducted using a potentiostat (Gamry Interface 1000) without any DC bias in a frequency range of  $10^6$  to  $10^{-2}$  Hz at 400 to  $600^{\circ}$ C. The AC amplitude used was 0.1 mA. The effect of oxygen partial pressure was tested by varying the flow rate of pure  $O_2$  versus pure  $N_2$  using mass flow controllers to achieve  $pO_2$  of 0.1, 0.2, 0.5, and 1 atm., while the effect of  $H_2O$  was tested by passing the simulated air through a water bubbler at room temperature and  $66^{\circ}$ C to achieve  $pH_2O$  of  $\sim 0.03$  and  $\sim 0.26$  atm., respectively. Each time the atmosphere was changed, there was a typical delay of 2.5 h before the electrochemical measurements could be taken. (Such a delay is based on our previous experiments, which showed that the impedance stabilizes after similar time. On the other hand, from the gas flow point of view, this delay is also reasonable because the total flow rate was maintained at 40cc/min. Over 2.5 h, the total flow volume is 6000 cc, which is much larger than the test chamber volume of  $\sim 100$  cc (2.5 cm ID, 20 cm long)).

# Results and discussion

# Fabricated patterned electrode cell

Figures 4 (a) and 4(b) show the layout editor design and a photograph, respectively, of an Ag patterned electrode fabricated over the BZCYYb4411 proton conducting electrolyte. The pattern has 4 long fingers and a wide busbar for current collection. The designed TPB length ( $L_{TPB}$ ) and

the electrode area ( $A_{ELT}$ ) were 30.4 mm and 15.3 mm<sup>2</sup>, respectively. Figures 4 (c) and 4(d) show a corresponding SEM micrograph and EDS line scan, respectively, of such a sample. The silver electrode is reasonably dense considering its thickness of only ~75 nm.

# Preliminary electrochemical test for patterned Ag electrode cell

Figure 5 shows the impedance spectra of a silver patterned electrode cell with PNC counter electrode in simulated air (<5 ppm H<sub>2</sub>O and CO<sub>2</sub> by volume, according to Airgas) as well as humidified air with pH<sub>2</sub>O of 0.03 and 0.26 atm. at 600-450°C. A previous study by the authors<sup>32</sup> has shown that porous PNC cathode over the same proton conducting electrolyte gives much lower interfacial resistance (about one tenth), which, as a first approximation, allows to neglect the contribution of PNC counter electrode in the current patterned Ag electrode cell.

On the other hand, in comparison with simulated air, the addition of 0.03 atm. of  $H_2O$  resulted in a reduction of ohmic resistance ( $R_O$ , the high frequency intercept in the impedance spectra) indicating higher bulk conductivity, particularly at temperatures of 600 and 550°C. This is attributed to the hydration of the BZCYYb4411 electrolyte and formation of proton ( $OH_{O}$ ) from oxygen vacancy, leading to higher ionic conductivity  $^{9,32}$ . As  $pH_2O$  further increased to 0.26 atm., there was almost no further change of  $R_O$  indicating saturation of hydration at 0.03 atm.

The electrode interfacial process can roughly be separated into two parts: a high-frequency resistance corresponding to the high frequency (HF) loops ( $\sim 10^6$  to  $10^4$  Hz) and a mid-to-low frequency (MF-LF) resistance, corresponding to multiple, partially overlapping loops in the mid to low frequency ( $\sim 10^4$  to  $10^{-3}$  Hz) range. With the introduction of 0.03 atm. of moisture, the HF loops of the EIS *decreased* for all temperature from 600 to 450°C. With increase of  $pH_2O$  to 0.26 atm., the HF loops decreased further, especially at lower temperature of 500°C or 450°C. It is

natural to expect that, in a simulated air atmosphere with very little moisture, ORR would proceed via the oxygen vacancy pathway (equation 1), while after the introduction of moisture and full hydration of the proton-conducting electrolyte, ORR would proceed via the proton pathway (equation 2). It is hypothesized that the charge transfer step, as often believed to be represented by the HF loops in the EIS, might be intrinsically *faster* for the proton route than the oxygen vacancy route. Such a hypothesis is consistent with earlier observations of depressed HF loops with increasing  $pH_2O$  for BSCF cathode over proton conducting electrolyte<sup>12</sup>.

On the other hand, with the introduction of moisture, the total apparent electrode interfacial resistance, R<sub>ai</sub>, (i.e., the direct difference between the high and low frequency intercepts on the impedance spectra) actually increased significantly, primarily due to the large expansion of the mid-to-low frequency MF-LF loops, and the increase is more significant when the moisture content is higher (0.26 atm. vs. 0.03 atm.). One possible explanation for such an observation is related to the reduced shorting effect based on the defect reaction involving electron hole (h\*) and protonic defect

$$2H_2O + 4O_0^{\times} + 4 h^{\bullet} \leftrightarrow O_2 + 4(OH)_0^{\bullet}$$
 (3)

, where an increase in  $pH_2O$  would shift the reaction to the right and reduce electron hole concentration, decreasing electronic leakage through the electrolyte<sup>44</sup>. Previous studies have shown that electronic leakage through proton conducting electrolytes, such as Y-doped BaCeO<sub>3</sub> or BaZr<sub>x</sub>Ce<sub>1-x</sub>O<sub>3</sub>, cause the apparent interfacial resistance R<sub>ai</sub> to be smaller than the actual values, particularly at high temperatures and high  $pO_2^{45,46}$ . As a result, reduced electronic leakage due to moisture introduction and hydration of the electrolyte would cause R<sub>ai</sub> to increase, even though the electrode kinetics might stay largely the same<sup>44,45</sup>. Another possibility is that, since the MF-LF loops in EIS are commonly associated with O<sub>2</sub> adsorption and dissociation processes<sup>12,13</sup>, their

observed increase might be attributed to the blockage of surface reaction sites by adsorbed  $H_2O$  molecules, in this case, near the TPB between Ag electrode and the BZCYYb4411 electrolyte, which reduces the active sites for  $O_2$  adsorption and dissociation. Which of the two explanations plays the dominant role needs to be investigated in future. It is worth mentioning that the Warburg-like behavior is observed at lower temperatures of 500 and 450°C under different atmospheric conditions, as well as at a higher temperature of 550°C with a higher  $pH_2O$  content of 0.26 atm. Warburg lines are often associated with diffusion (i.e., mass transport) limitations. At lower operating temperature (e.g., 450°C) or with higher  $pH_2O$  content (e.g.,  $pH_2O = 0.26$  atm.), it is hypothesized that the availability of oxygen atom becomes limited, possibly from slower oxygen dissociation or surface diffusion (e.g., to TPB), which result in the Warburg-like behavior. Of course, additional studies, especially computation modeling are needed to test such a hypothesis.

The impedance spectra are further analyzed using the Distribution of Relaxation Time (DRT) method  $^{47-54}$ , as shown in Figure 6. Multiple peaks (7+) are observed across different frequency ranges. Consistent observation (i.e., multiple processes for the electrode reaction) is obtained by fitting the EIS data to equivalent circuit using the ZView software. Supplementary Figure S1 shows the fittings for the EIS plot at 550°C in simulated air with water addition at  $pH_2O = 0.03$  atm., considering 4, 6, 7, and 8 RC circuits. It appears that 8 RC circuits provide the best fit, while 4 RC gives the worst fitting. Supplementary Figure S3 shows the fittings for the EIS plot in simulated air with water addition at  $pH_2O = 0.03$  atm. at 600-450°C. The fitted equivalent circuits turn out to contain 8-9 RC circuits in series. Such a number of RC elements seems high but still reasonable given the DRT plots in Fig.6 showing 7+ peaks. The high number is also possible due to the complex nature of the 4-electron ORR process and the many elemental steps that may be involved, as suggested in earlier studies  $^{14,15}$ .

On the other hand, there are still significant uncertainties in fittings. In addition, linking the elemental steps of the electrode reaction with the different peaks in DRT or the semi-circles in EIS is difficult due to the complex nature of the ORR process. In fact, with the limited information currently available, it is impossible at this stage. Therefore, both experiments and theoretical modeling are currently underway to deepen the understanding of the cathode ORR processes for proton conducting SOFC.

Nevertheless, Figure 7(a) shows electrode interfacial conductance, 1/R<sub>ai</sub>, normalized by TPB length vs. inverse of temperature (i.e., 1/T) for Ag patterned electrode over BZCYYb4411 proton conducting electrolyte in simulated air and in air with pH<sub>2</sub>O of 0.03 and 0.26 atm. at 600-450°C. For comparison, data from previous studies by Herle et al. 16 and Huang et al. 30 on Ag patterned electrodes in air over conventional oxygen ion conducting yttria-stabilized zirconia (YSZ) electrolyte, are also plotted. Despite the many differences between the current study and the one by Herle et al. 16, i.e., silver pattern geometry, electrolyte type (BZCYYb4411 proton conducting electrolyte vs. YSZ oxygen ion conducting electrolyte), and testing temperature, the measured interfacial conductance (1/R<sub>ai</sub>) normalized by TPB length appear to roughly fall on the same trend line for silver electrodes. In contrast, Huang et al.30 showed better activity for the Ag patterned electrode on YSZ from 550°C down to 450°C. Additionally, the activation energy of the current study is 0.93-0.98 eV, much lower than that of Herle et. Al<sup>16</sup> (1.19 eV) and Huang et al.<sup>30</sup> (1.65 eV) for Ag patterned electrode over oxygen ion conducting YSZ electrolyte. This suggests potentially better activity for Ag patterned electrode at temperature below 450°C over the proton conducting BZCYYb4411 electrolyte than YSZ electrolyte. Further study is needed to verify this.

To gain additional insights into the reaction process including possible rate limiting steps, reaction order analysis is often carried out<sup>14,15,55–60</sup>. Such an analysis may provide information

regarding the influence of different reactants' activity, such as the partial pressures of oxygen  $(pO_2)$ and water vapor (pH<sub>2</sub>O), on the rate of the ORR. According to literature, the overall reaction rate, or the inverse of electrode apparent interfacial resistance depends on oxygen and water vapor pressure:  $1/R_{ai} \propto (pO_2)^n \cdot (pH_2O)^m$ , where n and m are reaction order for  $pO_2$  and  $pH_2O$ , respectively. The cathode reaction involves several fundamental steps for proton conducting SOFC: 1. Oxygen adsorption, 2. Oxygen dissociation, 3. Charge transfer (multiple steps, actually), 4. Water formation, and 5. Desorption of water  $^{14,15}$ . By plotting  $1/R_{ai}$  against  $pO_2$  or  $pH_2O$  (both in logarithmic scale), the reaction order (n or m value) might be obtained from the fitted slope of the plot. Figure 7(b) shows plots of  $\log(1/(R_{ai}*L_{TPB}))$  vs.  $\log(pH_2O)$  for patterned Ag cathode at different temperatures from 600 to 450°C. The obtained reaction order with respect to  $pH_2O$ , m, is -0.14 to -0.22. These values fall outside the range of m (0.5-1) modeled in previous studies. On the other hand, these numbers are very close to the value (-0.21) obtained for  $La_{0.6}Sr_{0.4}Co_{0.2}Fe_{0.8}O_{3-\delta}$  (LSCF) cathode over  $BaCe_{0.9}Y_{0.1}O_{3-\delta}$  (BCY10) proton conducting electrolyte at 600°C<sup>15</sup>. Whether such a consistency is pure co-incidence given the difference in electrode and electrolyte materials or the two cells are indeed limited by the same fundamental process (e.g., electronic leakage effect in the proton conducting electrolyte) needs to be studied in future.

Figure 8 shows the impedance spectra of the Ag patterned electrode cell in various  $pO_2$  (0.1, 0.2, 0.5, and 1 atm.) at 600-450°C. The bulk or ohmic resistance decreases with increasing temperature, which is expected for solid oxide fuel cells. The primary factor contributing to the observed drop in ohmic resistance with increasing temperature is the higher mobility for the charge carriers (oxygen vacancy or protons, if water is present) at higher temperature. It is also expected that the cell's ohmic resistance would be independent of the electrode's architecture, whether

porous or dense, and should show the decrease with temperature. This was indeed observed in the current study: the *area corrected* ohmic resistance for the Ag patterned electrode cell matches very well with our earlier study using a porous electrode over the same  $BaZr_{0.4}Ce_{0.4}Y_{0.1}Yb_{0.1}O_{3-\delta}$  (BZCYYb4411) electrolyte <sup>32</sup>.

On the other hand, at 600 and 550°C, ohmic resistance  $R_0$  increased as  $pO_2$  decreased from 1 to 0.1 atm., which is attributed to the decrease in the electronic conduction (or leakage) of the BZCYYb4411 electrolyte resulting from a drop in  $pO_2$ : Based on the defect reaction involving oxygen vacancy and electron hole:

$$2 O_0^{\times} + 4 h^{\bullet} \leftrightarrow O_2 + 2 V_0^{\bullet}$$
 (4)

a drop in  $pO_2$  would shift the reaction to the right and reduce electron hole concentration. At 500 and 450°C, there is almost no change in  $R_O$ . This is likely because hole conduction is significantly less at lower temperature for electrolytes that display electronic leakage (e.g., acceptor-doped  $CeO_2$  and  $BaCeO_3$ )<sup>46</sup>. (In comparison, previous studies have shown that small change in  $pO_2$  has no obvious effect on  $R_O$  for oxygen ion-conducting YSZ electrolyte, as the electronic conduction in YSZ is negligible under similar condition <sup>28,61</sup>.)

Meanwhile, with reduced  $pO_2$ , there is an increase in total apparent electrode interfacial resistance  $R_{ai}$ . Such a behavior (increase of  $R_{ai}$  with reduced  $pO_2$ ) is consistent with porous Ag cathode symmetrical cell over  $BaZr_{0.1}Ce_{0.7}Y_{0.1}Yb_{0.1}O_{3-\delta}$  (BZCYYb1711) proton conducting electrolyte<sup>13</sup> and is expected to come from a slowdown in oxygen gas phase transport, surface adsorption, and dissociation with lower oxygen concentration. In addition, the reduced electronic leakage, due to shifting of reaction (4) to the right with lower  $pO_2$ , especially at higher temperature such as 600 and 550°C, is also expected to contribute to the increase in  $R_{ai}^{62}$ . Interestingly, at elevated temperatures such as 600 and 550°C, there appears to be a continuation of the EIS loop

at the low frequency end towards the real axis. The exact reason is not clear. One possibility is that, at these temperatures, the ORR elemental steps such as O<sub>2</sub> dissociative adsorption might be much faster than at a lower temperature (i.e., 450°C). This might enable the presence of surface active species even under very low frequency (near DC condition) and the continuation of the EIS loop towards the real axis instead of the Warburg-like behavior seen at lower temperatures such as 450°C.

Figure 9 are DRT curves for impedance spectra shown in Figure 8. Similar to the testing in simulated air (see Figure 6), multiple peaks (7+) are also observed across the frequency range. Like before, the supplementary Figure S2 shows the fittings for the EIS plot at 550°C in dry 20%  $O_2$ -80%  $N_2$  mixture (i.e.,  $pO_2 = 0.2$  atm.), considering 4, 5, 6, and 8 RC circuits. In this case, 6 RC circuits seem to be enough to give a reasonable fit, while the fitting with 4 RC gives unsatisfactory results. Supplementary Figure S4 shows the fittings for the EIS plot in dry 20%  $O_2$ -80%  $N_2$  mixture (i.e.,  $pO_2 = 0.2$  atm.) at 600-450°C. The fitted equivalent circuits turn out to contain 6-8 RC circuits in series. As explained before, such a high number of peaks is probably due to the complex nature of the 4-electron ORR process involving many elemental steps.

Fig. 10 shows inverse of  $R_{ai}$  normalized by TPB length vs.  $pO_2$  plot, both in logarithm scale for the Ag patterned electrode cell over BZCYYb4411 proton conducting electrolyte in this study at 600-450°C in comparison to dense Ag electrode by Herle et al. at 753°C<sup>16</sup>, and by Huang et al.<sup>30</sup> at 450°C, all over conventional YSZ electrolyte. For current dense Ag patterned electrode over proton conducting electrolyte,  $1/R_{ai}$  increases with increasing  $pO_2$  for all temperature from 600 to 450°C, with roughly the same slope, indicating that the same rate-controlling mechanism. The fitted slope n is in the range of 0.39-0.47, which indicates the ORR process on Ag electrode over BZCYYb4411 proton conducting electrolyte is likely controlled by both oxygen dissociation (n =

0.5) and charge transfer (n = 0.25), according to earlier study by Grimaud et al<sup>15</sup>. Further study is needed to confirm this.

In addition to the studies discussed above, new experiments are currently underway involving the fabrication of dense patterned Ag electrodes with different TPB lengths and electrode contact areas to clarify the relationship between geometric parameters (e.g., L<sub>TPB</sub>) and electrode kinetics for ORR over proton conducting electrolyte. Reference electrode will also be added to the patterned electrode cell to get polarization curves. More systematic studies with respect to atmosphere and bias conditions will also be carried out. Additionally, Ag patterned electrodes with the same electrode geometry will be fabricated over both proton conducting and oxygen ion conducting electrolytes with comparable total ionic conductivity (e.g., BZCYYb4411 and GDC at ~450°C in simulated air). This will allow for another angle to examine the roles of proton conducting electrolyte in the critical ORR versus conventional oxygen conducting electrolyte. Last, but not the least, theoretical calculations using both density functional theory (DFT) method and electrochemical modeling based on finite element method (FEM) will be conducted to reveal the cathode ORR reaction mechanism including all the elemental steps for proton conducting SOFC.

#### **Conclusions**

In this study, Ag patterned cathodes were successfully fabricated on BZCYYb4411 proton conducting electrolyte by photolithography and E-beam evaporation. Electrochemical cells with the fabricated Ag patterned working electrode and PNC counter electrode were tested for electrochemical impedance spectroscopy. The results show for Ag metal cathode over proton conducting electrolyte, with the introduction of moisture to air, both ohmic resistance and EIS high frequency loop decrease, representing bulk hydration and change of reaction pathway from oxygen

ion to proton, while the mid-to-low frequency loops increase, possibly due to either water adsorption blocking  $O_2$  adsorption/dissociation and diffusion to the TPB or reduced electronic leakage through the electrolyte. In addition, decreasing  $pO_2$  also appears to slow the cathode process in a way similar to moisture effect. The reaction order in terms of interfacial conductance is estimated to be in the range of -0.14 to -0.22 for moisture and 0.39 to 0.47 for oxygen. Analysis of the EIS data by both the DRT analysis and fitting to equivalent circuits suggest multiple elemental steps reflecting the complex nature of the cathode ORR reaction, especially when water and proton are involved. Future work, involving both experiments and theoretical calculations (e.g., by finite element electrochemical modeling and DFT calculation), will focus on revealing the effects of patterned electrode geometry on electrode kinetics and the fundamental mechanism (especially pathway) of ORR for proton conducting IT-SOFC.

# **CRediT** authorship contribution statement

Md Shariful Islam Sozal: Methodology, Investigation, Data curation, Writing – original draft. Wenhao Li: Methodology. Suprabha Das: Methodology. Borzooye Jafarizadeh: Methodology. Azmal Huda Chowdhury: Methodology. Chunlei Wang: Methodology. Zhe Cheng: Conceptualization, Funding, Supervision, Writing – review & editing.

# **Declaration of competing interest**

There are no conflicts to declare.

# Acknowledgment

This research is supported by the National Science Foundation (Award No. DMR-1848305). The use of facilities at FIU Advanced Materials Engineering Research Institute (AMERI) and Dr. John

T. Macdonald Foundation Biomedical Nanotechnology Institute (BioNIUM) Nanofabrication Facility of University of Miami are acknowledged. The Dissertation Acquisition Fellowship (DEA) from FIU is also acknowledged for its valuable support.

Materials Advances Page 66 of 87

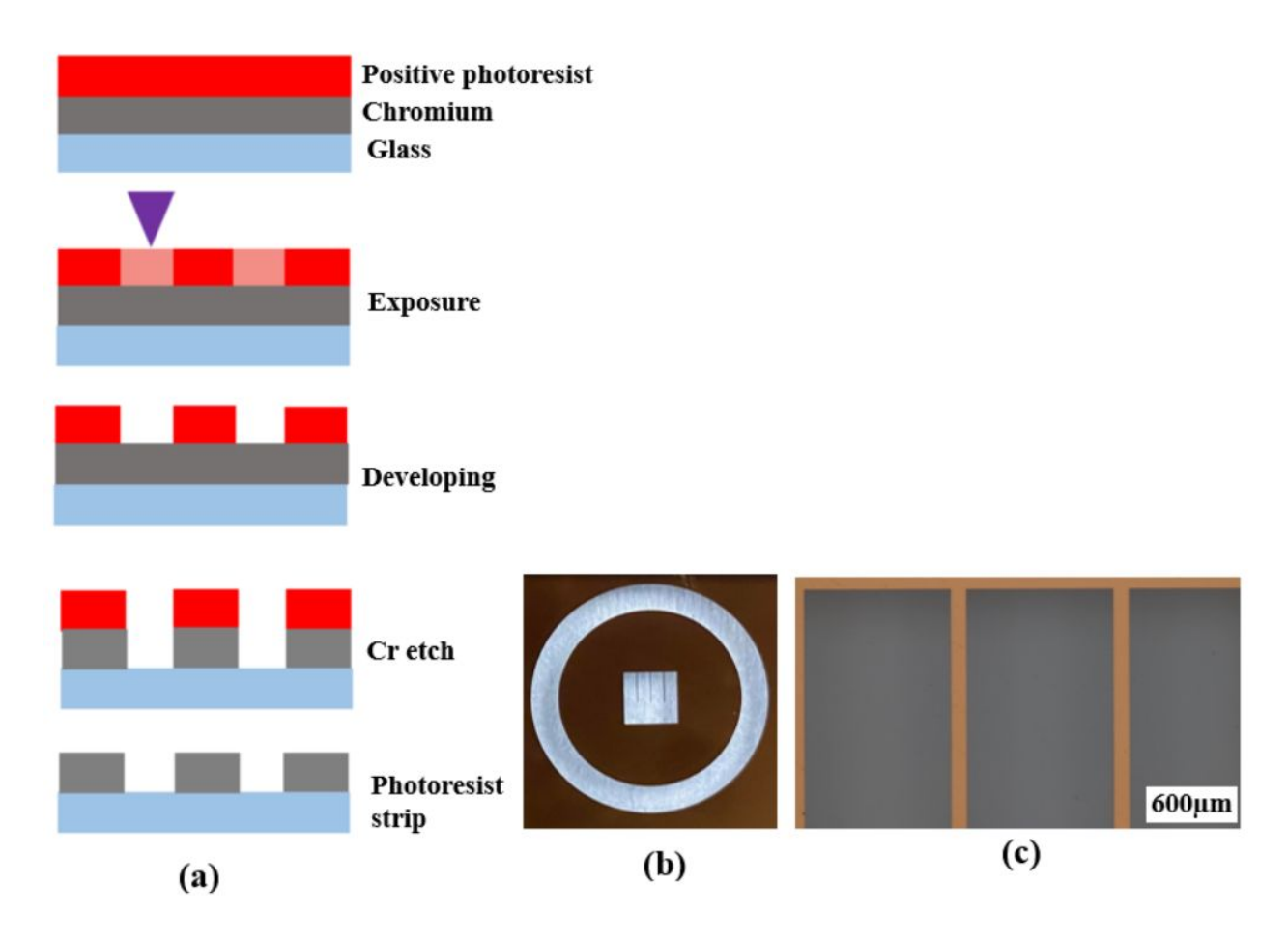


Fig. 1: (a) Schematic representation of the fabrication process of the photomask (b) photograph of the final photomask (c) microscopic image of the photomask, showing the fine features and patterns.

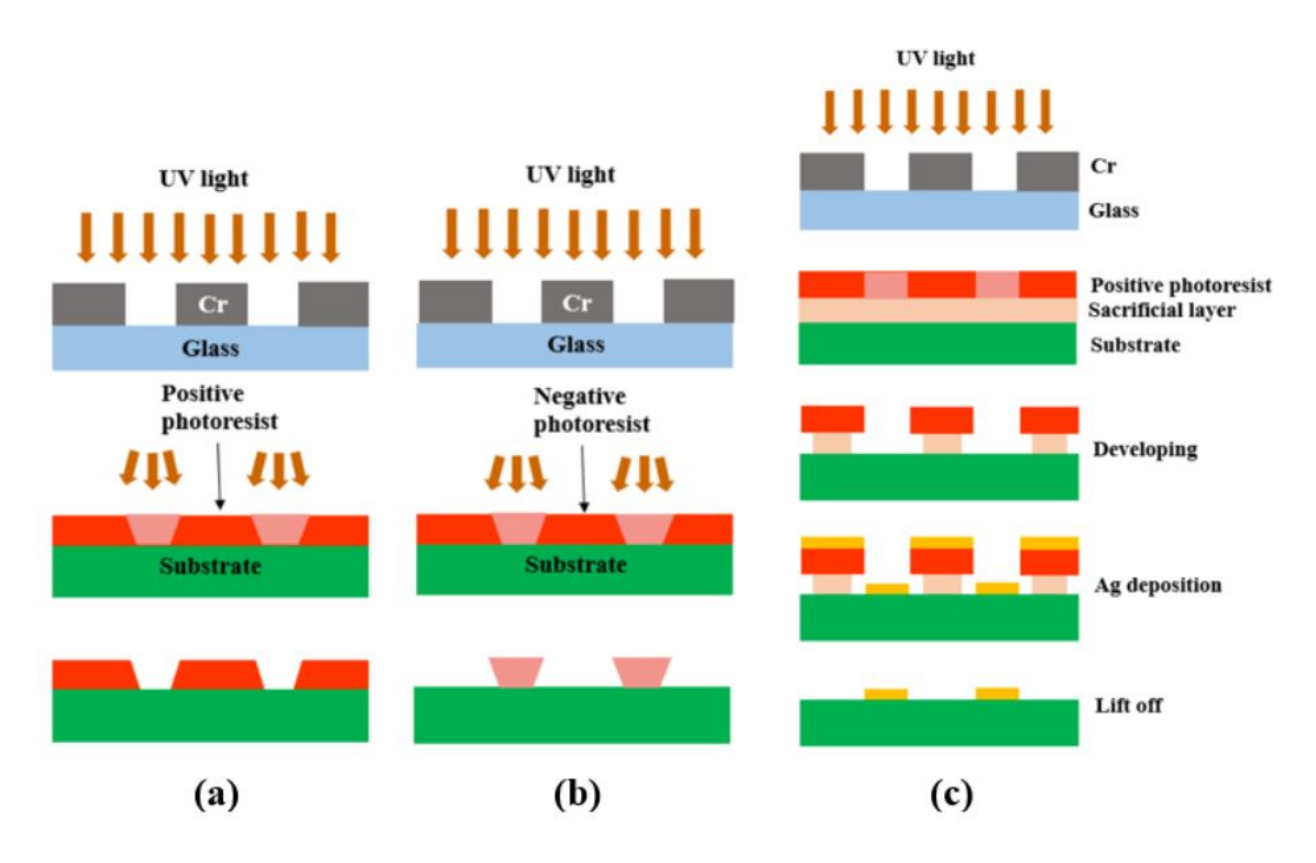


Fig. 2: Schematic showing (a) overcut profile formed in positive photoresist, with wider opening at the photoresist top surface than at the bottom or near the substrate <sup>39</sup>, (b) undercut profile formed in negative photoresist, with narrower opening at the photoresist top surface than at the bottom or near the substrate <sup>39</sup>, and (c) photolithography process using a bilayer resist system.

Materials Advances Page 68 of 87

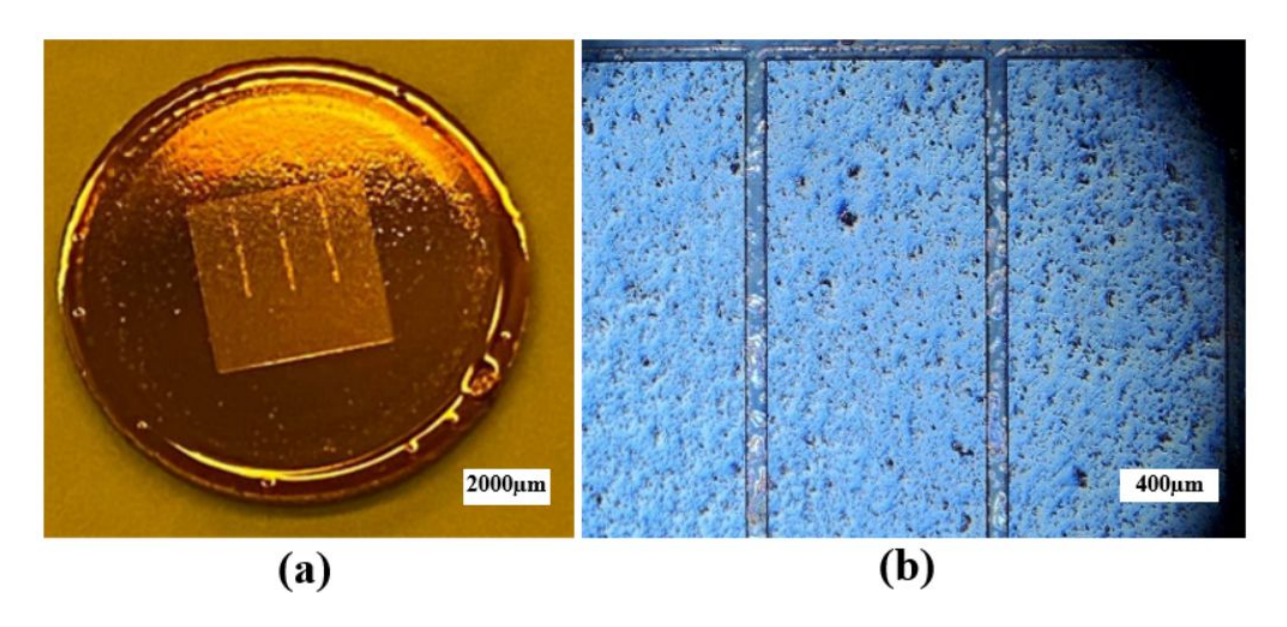


Fig. 3: (a) Photograph and (b) optical microscopic image of the BZCYYb4411 electrolyte substrate covered by patterned photoresist after development.

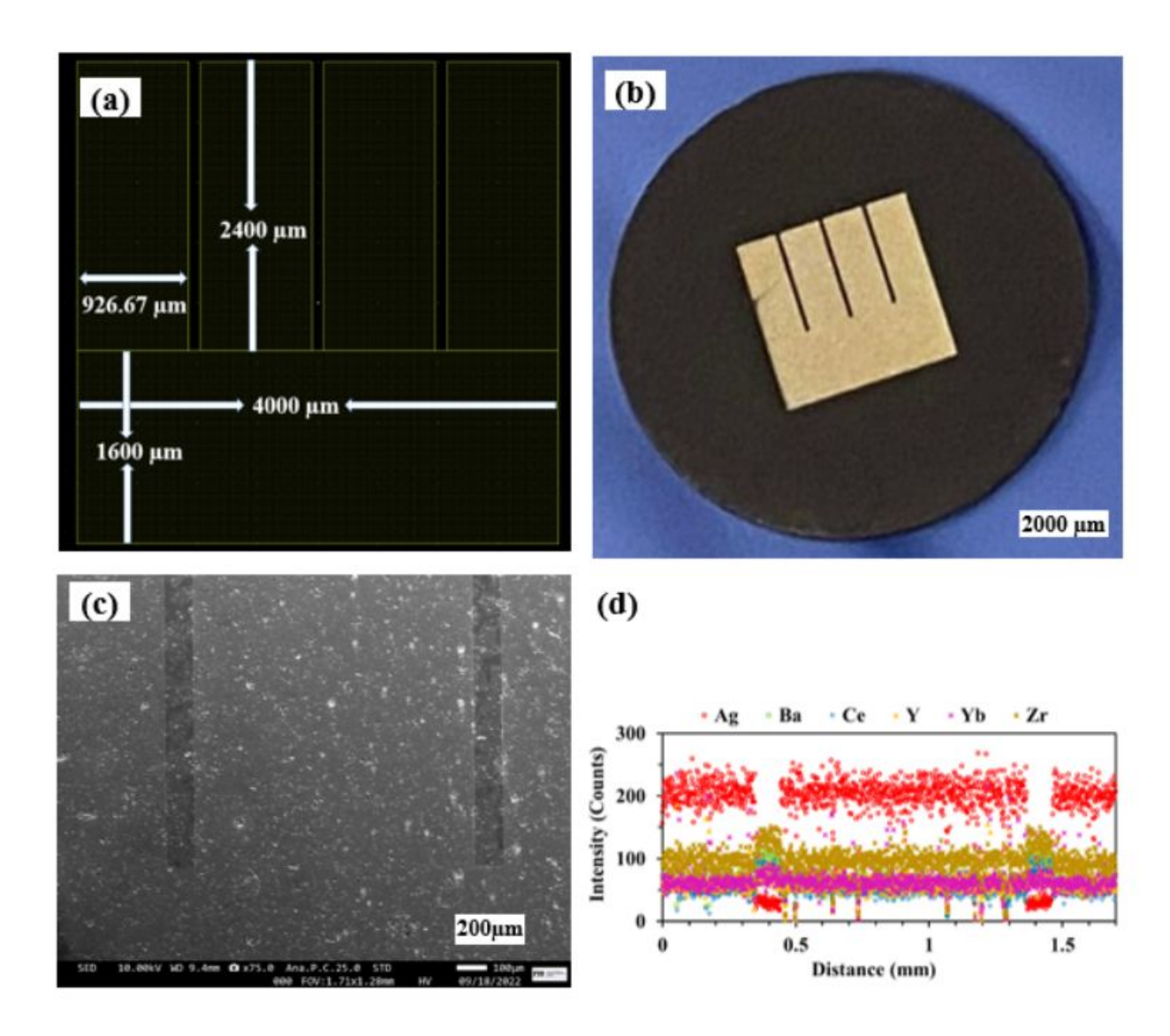


Fig. 4: (a) The Layout Editor design, (b) photograph, (c) SEM micrograph, and (d) EDS line scan of Ag patterned electrode over BZCYYb4411 electrolyte substrate.

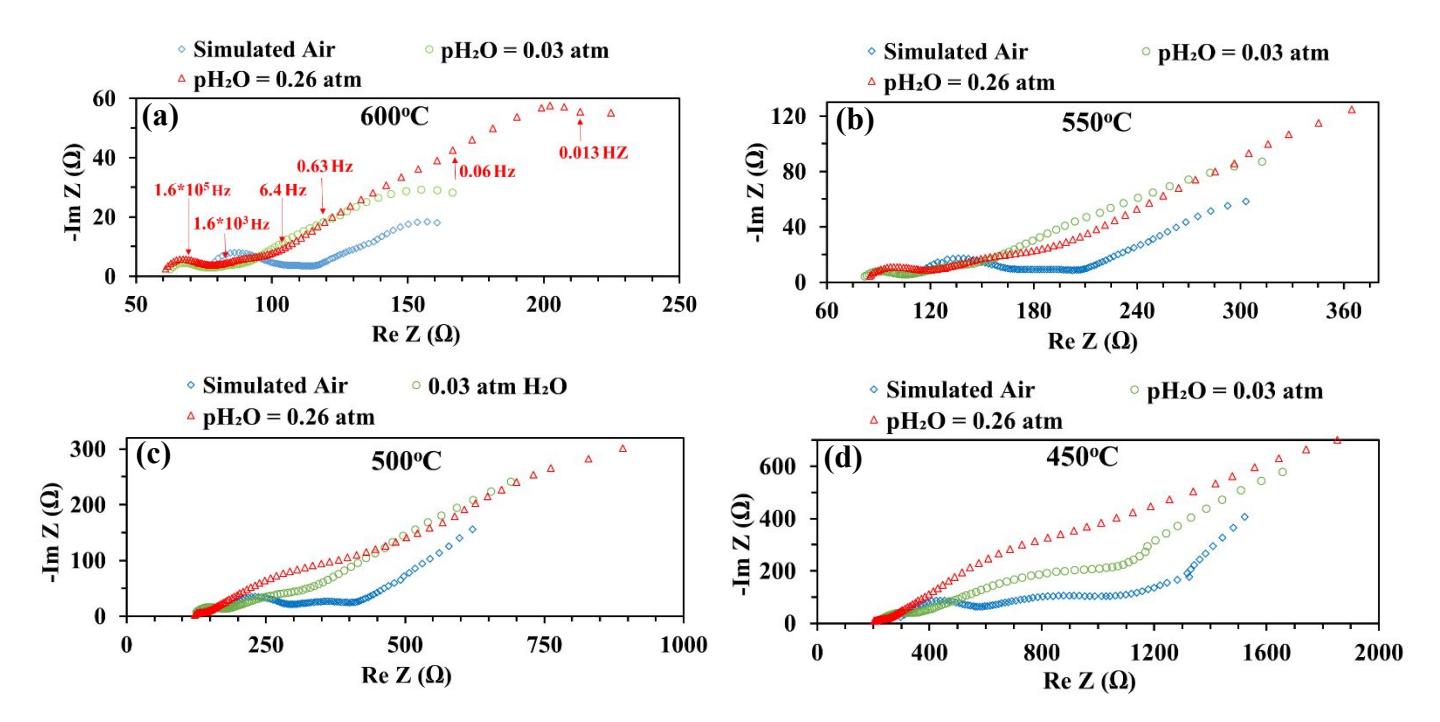


Figure 5: Plots of EIS for an electrochemical cell with patterned Ag working electrode over BZCYYb4411 proton conducting electrolyte and PNC counter electrode in simulated air and in various  $pH_2$ O level of 0.03 and 0.26 atm. at (a) 600, (b) 550, (c) 500, and (d) 450°C, respectively.

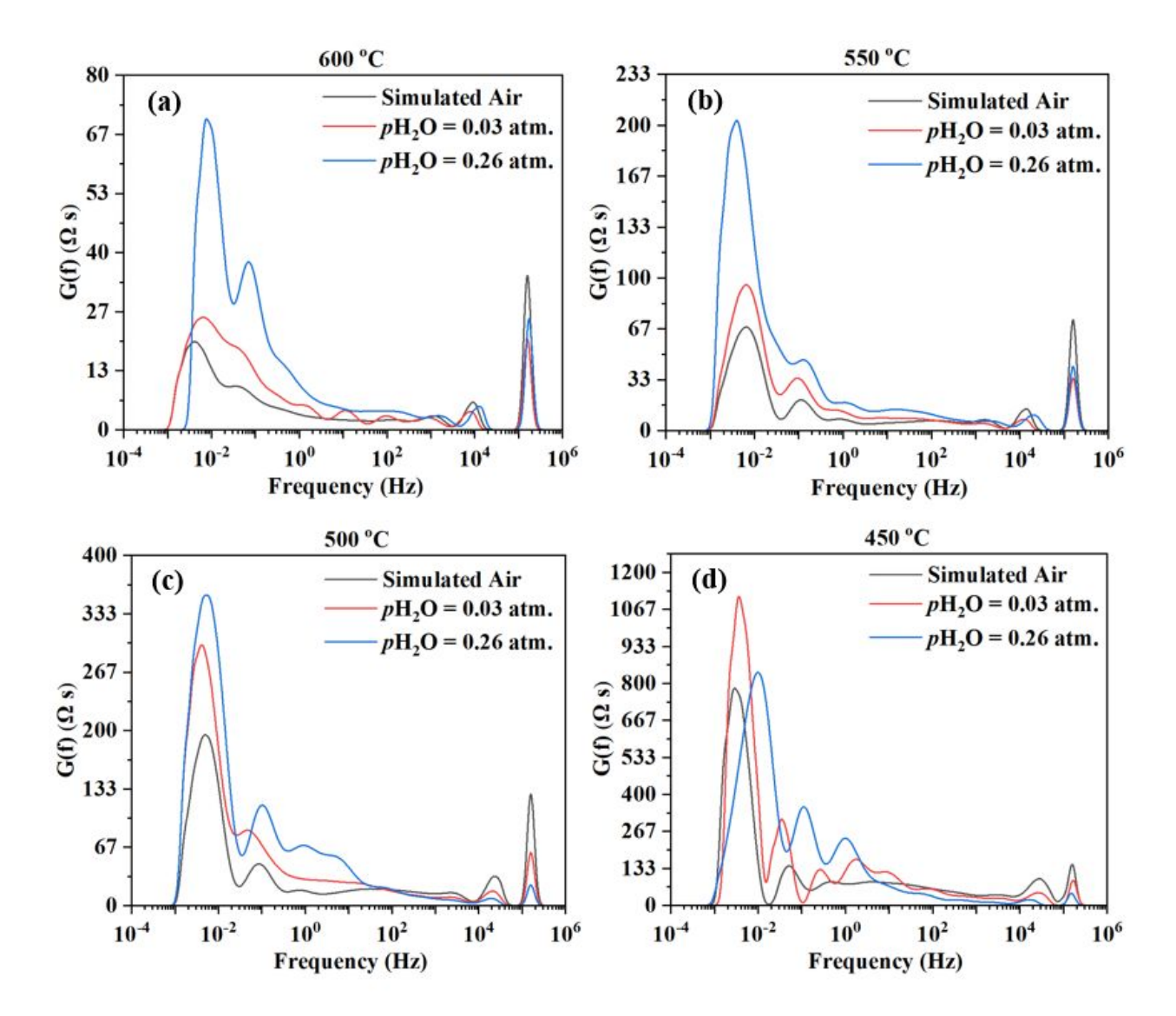


Figure 6: Distribution of relaxation times (DRT) curves from impedance spectra for an electrochemical cell with patterned Ag working electrode, BZCYYb4411 proton conducting electrolyte, and PNC counter electrode in simulated air (<5 ppm  $H_2O$  and  $CO_2$  according to Airgas) and with added  $pH_2O$  of 0.03 and 0.26 atm. at (a) 600, (b) 550, (c) 500, and (d) 450°C, respectively.

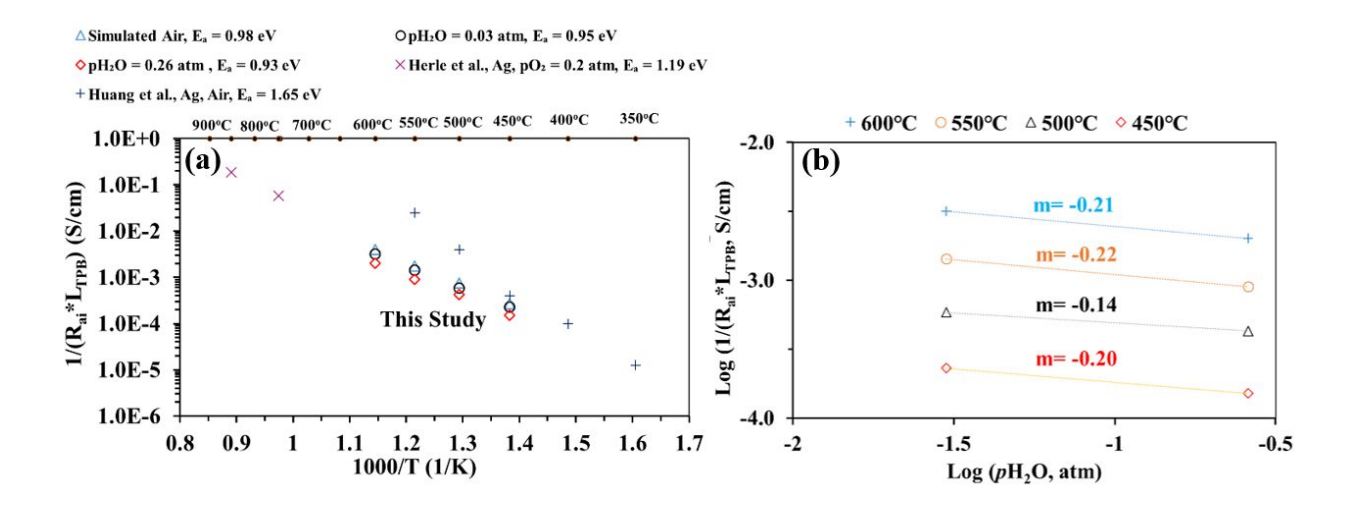


Figure 7 (a) Plot of inverse of  $R_{ai}$  normalized by TPB length versus inverse temperature for the Ag patterned electrode cell over BZCYYb4411 proton conducting electrolyte in simulated air, and in air with  $pH_2O$  of 0.03 and 0.26 atm. at 600-450°C. The results from previous studies by Herle et al. and Huang et al. on Ag patterned electrodes, all in air over oxygen ion conducting yttriastabilized zirconia (YSZ) electrolyte are also shown for comparison. (b) Inverse of  $R_{ai}$  normalized by TPB length vs.  $pH_2O$  plot, both in logarithm scale, showing the fitted reaction order m with respect to  $pH_2O$  for patterned Ag cathode over BZCYYb4411 electrolyte at 600-450°C.

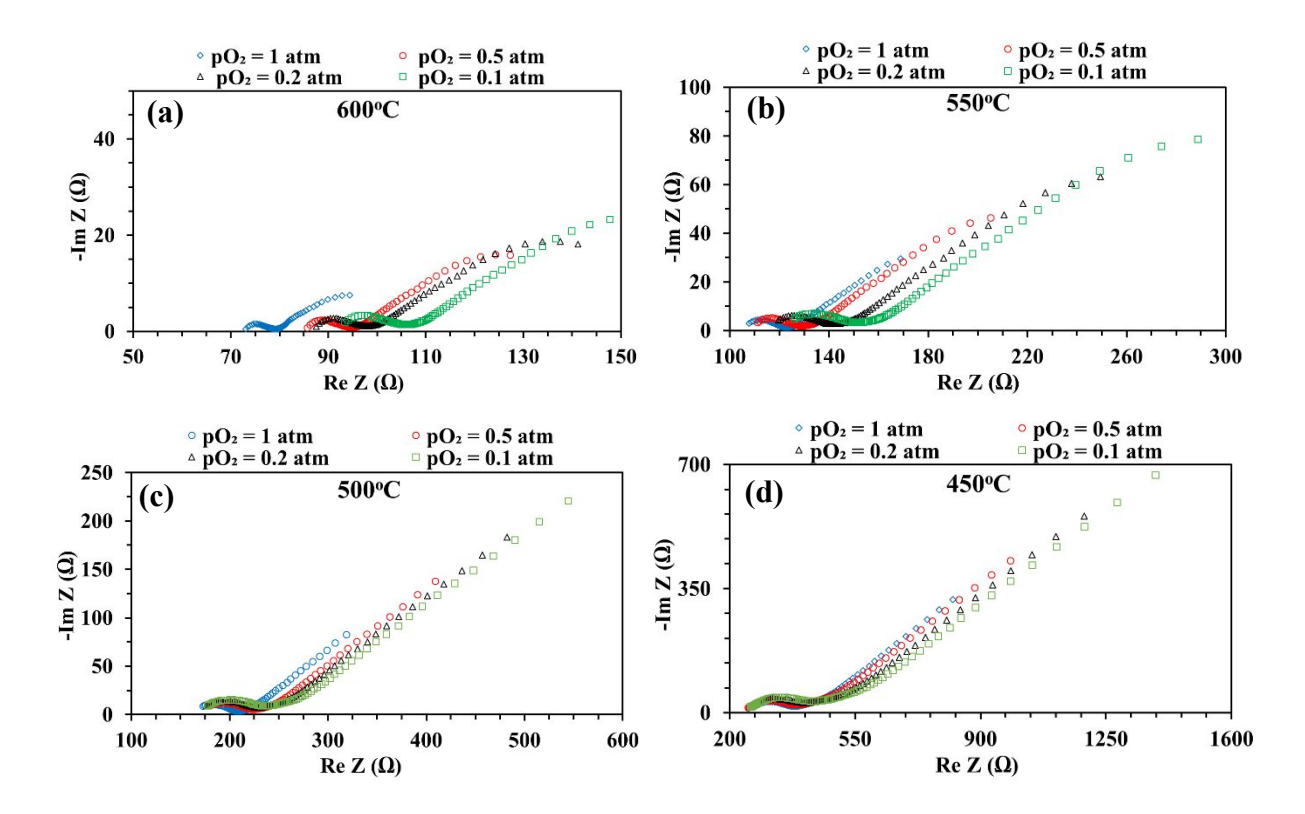


Figure 8: Electrochemical impedance spectra (EIS) for an electrochemical cell with patterned Ag working electrode and PNC counter electrode in  $O_2$ - $N_2$  mixture with  $pO_2$  of 1, 0.5, 0.2, and 0.1 atm. at (a) 600, (b) 550, (c) 500, and (d) 450°C, respectively.

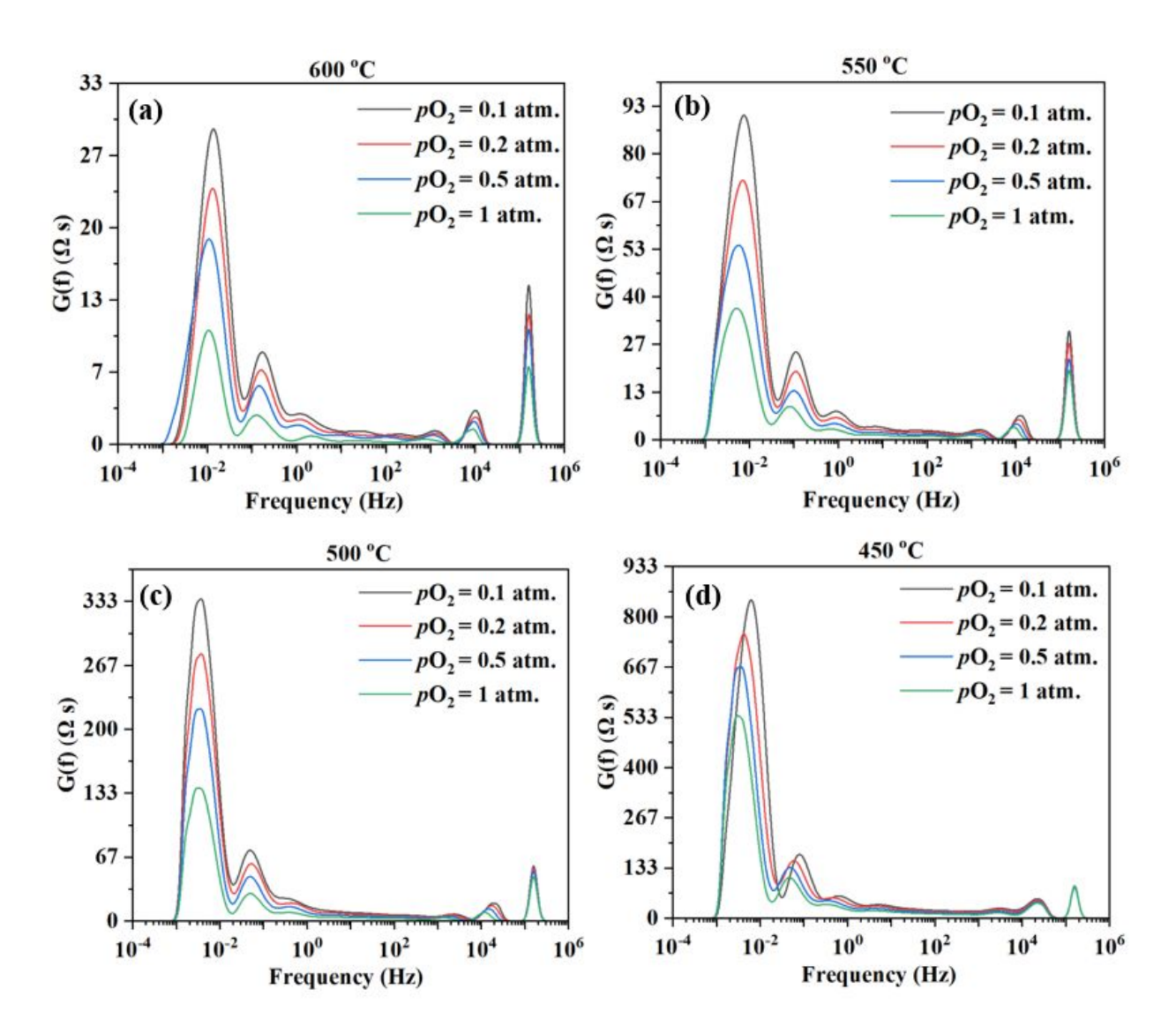


Figure 9: Distribution of Relaxation Times (DRT) curves of impedance spectra for an electrochemical cell with patterned Ag working electrode and PNC counter electrode in  $O_2$ - $N_2$  mixture with  $pO_2$  of 0.1, 0.2, 0.5, and 1 atm. at (a) 600, (b) 550, (c) 500, and (d) 450°C, respectively.

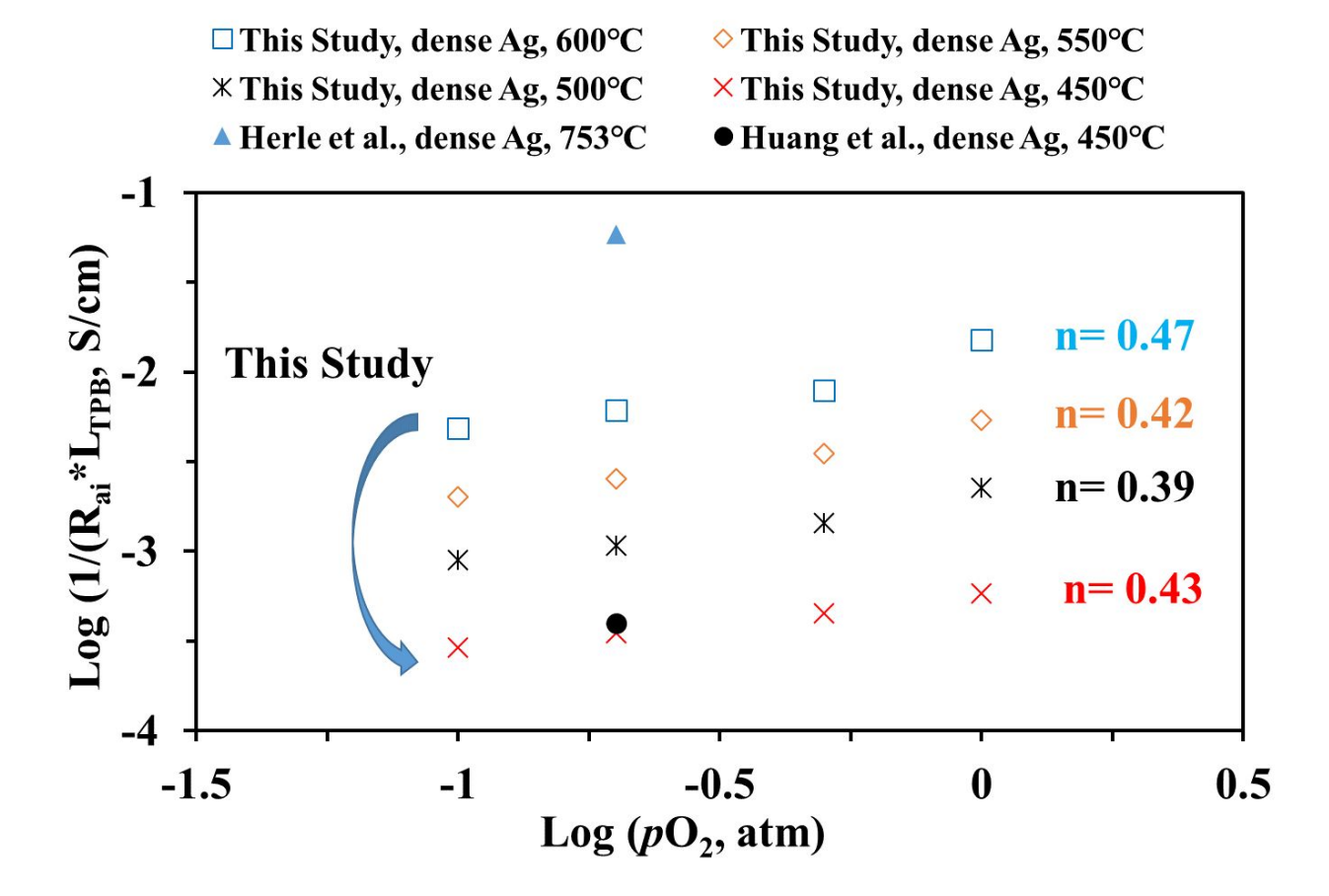


Fig. 10 (a): Plot of log ( $1/(R_{ai}*L_{TPB})$  vs. log ( $pO_2$ ) for the dense Ag patterned electrode over proton conducting BZCYYb4411 electrolyte in this study. Data for dense Ag patterned electrode over YSZ electrolyte by Herle et al.<sup>16</sup> at 753°C, and Huang et al.<sup>30</sup> at 450°C are also shown for comparison.

#### References

- 1. Minh, N. Q. Ceramic Fuel Cells. J. Am. Ceram. Soc. 76, 563–588 (1993).
- 2. Singhal, S. C. Solid oxide fuel cells for stationary, mobile, and military applications. *Solid State Ionics* **152–153**, 405–410 (2002).
- 3. Lu, C., An, S., Worrell, W. L., Vohs, J. M. & Gorte, R. J. Development of intermediate-temperature solid oxide fuel cells for direct utilization of hydrocarbon fuels. *Solid State Ionics* **175**, 47–50 (2004).
- 4. Singh, P. & Minh, N. Q. Solid oxide fuel cells: Technology status. *Int. J. Appl. Ceram. Technol.* 1, 5–15 (2004).
- 5. Wachsman, E. & Lee, K. Lowering the Temperature of Solid Oxide Fuel Cells. *Science* (80-.). **334**, 935–940 (2011).
- 6. Singh, M., Zappa, D. & Comini, E. Solid oxide fuel cell: Decade of progress, future perspectives and challenges. *Int. J. Hydrogen Energy* **46**, 27643–27674 (2021).
- 7. Yamazaki, Y., Hernandez-Sanchez, R. & Haile, S. M. High total proton conductivity in large-grained yttrium-doped barium zirconate. *Chem. Mater.* **21**, 2755–2762 (2009).
- 8. Guo, Y., Lin, Y., Ran, R. & Shao, Z. Zirconium doping effect on the performance of proton-conducting BaZryCe0.8-yY0.2O3- $\delta$  (0.0  $\leq$  y  $\leq$  0.8) for fuel cell applications. *J. Power Sources* **193**, 400–407 (2009).
- 9. Yang, L. *et al.* Enhanced Sulfur and Coking Tolerance of a Mixed Ion Conductor for SOFCs: BaZr0.1Ce0.7Y0.2–xYbxO3–d. **326**, 126–129 (2009).
- 10. An, H. et al. A  $5 \times 5$  cm2 protonic ceramic fuel cell with a power density of 1.3 W cm-2

- at 600 °C. Nat. Energy 3, 870–875 (2018).
- 11. Duan, C., Huang, J., Sullivan, N. & O'Hayre, R. Proton-conducting oxides for energy conversion and storage. *Appl. Phys. Rev.* **7**, 011314-(1-38) (2020).
- 12. Sun, S. & Cheng, Z. Effects of H2O and CO2 on Electrochemical Behaviors of BSCF Cathode for Proton Conducting IT-SOFC Effects of H2O and CO2 on Electrochemical Behaviors of BSCF Cathode for Proton Conducting IT-SOFC. *J. Electrochem. Soc.* 164, F81–F88 (2017).
- Sun, S. & Cheng, Z. Electrochemical Behaviors for Ag, LSCF and BSCF as Oxygen Electrodes for Proton Conducting IT-SOFC Electrochemical Behaviors for Ag, LSCF and BSCF as Oxygen Electrodes for Proton Conducting IT-SOFC. *J. Electrochem. Soc.* 164, F3104–F3113 (2017).
- 14. He, F., Wu, T., Peng, R. & Xia, C. Cathode reaction models and performance analysis of Sm0.5Sr0.5CoO3-δ-BaCe0.8Sm0.2O3-δ composite cathode for solid oxide fuel cells with proton conducting electrolyte. *J. Power Sources* **194**, 263–268 (2009).
- 15. Grimaud, A. *et al.* Hydration Properties and Rate Determining Steps of the Oxygen Reduction Reaction of Perovskite-Related Oxides as H+-SOFC Cathodes. *J. Electrochem. Soc.* **159**, 683–694 (2012).
- Van Herle, J. & McEvoy, A. J. OXYGEN DIFFUSION THROUGH SILVER
   CATHODES FOR SOLID OXIDE FUEL CELLS. J. Phys. Chem. Solids 55, 339–347
   (1994).
- 17. Brichzin, V., Fleig, J., Habermeier, H. U. & Maier, J. Geometry Dependence of Cathode

- Polarization in Solid Oxide Fuel Cells Investigated by Defined Sr-Doped LaMnO3 Microelectrodes. *Electrochem. Solid-State Lett.* **3**, 403–406 (2000).
- 18. Fleig, J., Kim, H. R., Jamnik, J. & Maier, J. Oxygen Reduction Kinetics of Lanthanum Manganite (LSM)Model Cathodes: Partial Pressure Dependence and Rate-Limiting Steps. *Fuel Cells* **8**, 330–337 (2008).
- Opitz, A. K. & Fleig, J. Investigation of O2 reduction on Pt/YSZ by means of thin film microelectrodes: The geometry dependence of the electrode impedance. *Solid State Ionics* 181, 684–693 (2010).
- 20. Kim, Y. B. *et al.* Nanopore Patterned Pt Array Electrodes for Triple Phase Boundary Study in Low Temperature SOFC. *J. Electrochem. Soc.* **157**, B1269–B1274 (2010).
- 21. Shim, J. H. *et al.* Patterned Silver Nanomesh Cathode for Low-Temperature Solid Oxide Fuel Cells. *J. Electrochem. Soc.* **159**, B541–B545 (2012).
- 22. Brichzin, V., Fleig, J., Habermeier, H. U., Cristiani, G. & Maier, J. The geometry dependence of the polarization resistance of Sr-doped LaMnO3 microelectrodes on yttria-stabilized zirconia. *Solid State Ionics* **152–153**, 499–507 (2002).
- 23. Hertz, J. L. & Tuller, H. L. Electrochemical Characterization of Thin Films for a Micro-Solid Oxide Fuel Cell. *J. Electroceramics* **13**, 663–668 (2004).
- 24. Koep, E., Mebane, D. S., Das, R., Compson, C. & Liu, M. Characteristic thickness for a dense La0.8Sr0.2MnO3 electrode. *Electrochem. Solid-State Lett.* **8**, A592–A595 (2005).
- 25. Fleig, J. *et al.* Thin Film Microelectrodes in SOFC Electrode Research. *Fuel Cells* **6**, 284–292 (2006).

- 26. Wang, J.-H., Liu, M. & Lin, M. C. Oxygen reduction reactions in the SOFC cathode of Ag/CeO2. *Solid State Ionics* **177**, 939–947 (2006).
- 27. Hertz, J. L. & Tuller, H. L. Measurement and finite element modeling of triple phase boundary-related current constriction in YSZ. *Solid State Ionics* **178**, 915–923 (2007).
- 28. Koc, S., La O', G. J., Golfinopoulos, T. & Shao-Horn, Y. Impedance Spectroscopy Studies of Oxygen Reduction Reaction on Thin Film Platinum Microelectrodes Supported on YSZ. *ECS Trans.* **7**, 1271–1277 (2007).
- 29. Baumann, F. S. *et al.* Quantitative Comparison of Mixed Conducting SOFC Cathode Materials by Means of Thin Film Model Electrodes. *J. Electrochem. Soc.* **154**, B931–B941 (2007).
- 30. Huang, H., Holme, T. & Prinz, F. B. Oxygen Reduction Characteristics on Ag, Pt, and Ag-Pt Alloys in Low Temperature SOFCs. in *E C S Transactions* vol. 3 31–40 (2007).
- 31. Choi, S. *et al.* Exceptional power density and stability at intermediate temperatures in protonic ceramic fuel cells. *Nat. Energy* **3**, 202–210 (2018).
- 32. Sozal, M. S. I. *et al.* Electrical, thermal, and H2O and CO2 poisoning behaviors of PrNi0.5Co0.5O3-δ electrode for intermediate temperature protonic ceramic electrochemical cells. *Int. J. Hydrogen Energy* **47**, 21817–21827 (2022).
- 33. Bieberle, A., Meier, L. P. & Gauckler, L. J. The Electrochemistry of Ni Pattern Anodes Used as Solid Oxide Fuel Cell Model Electrodes. *J. Electrochem. Soc.* **148**, A646–A656 (2001).
- 34. Ehn, A. et al. Electrochemical Investigation of Nickel Pattern Electrodes in H2/H2O and

- CO/CO2 Atmospheres. J. Electrochem. Soc. 157, B1588–B1596 (2010).
- 35. Yao, W. & Croiset, E. Ni/YSZ pattern anodes fabrication and their microstructure and electrochemical behavior changes in H2-H2O environments. *J. Power Sources* **226**, 162–172 (2013).
- 36. Li, W., Shi, Y., Luo, Y., Wang, Y. & Cai, N. Carbon deposition on patterned nickel/yttria stabilized zirconia electrodes for solid oxide fuel cell/solid oxide electrolysis cell modes. *J. Power Sources* **276**, 26–31 (2015).
- 37. Cherry, O. Fabrication of an Atom Chip for Rydberg Atom-Metal Surface Interaction Studies. *Master Thesis, Univ. Waterloo, Waterloo, Canada* (2007).
- 38. Zaouk;, R., Park;, B. Y. & Madou, M. J. Introduction to Microfabrication Techniques. *Methods Mol. Biol.* **321**, 5–15 (2010).
- 39. Marin, G. Inclined lithography and photoresist optimization for fabrication of 3D mesh structures. *Master Thesis, Aalto Univ.* 74 (2014).
- 40. Shaw, J. M., Gelorme, J. D., LaBianca, N. C., Conley, W. E. & Holmes, S. J. Negative photoresists for optical lithography. *IBM J. Res. Dev.* **41**, 81–94 (1997).
- 41. Lee, H. S. & Yoon, J. B. A simple and effective lift-off with positive photoresist. *J. Micromechanics Microengineering* **15**, 2136–2140 (2005).
- Lawson, R. A., Tolbert, L. M., Younkin, T. R. & Henderson, C. L. Negative-tone molecular resists based on cationic polymerization. *Adv. Resist Mater. Process. Technol.* XXVI 7273, 72733E1-72733E10 (2009).
- 43. Koep, E., Compson, C., Liu, M. & Zhou, Z. A photolithographic process for investigation

- of electrode reaction sites in solid oxide fuel cells. *Solid State Ionics* **176**, 1–8 (2005).
- 44. Poetzsch, D., Merkle, R. & Maier, J. Investigation of oxygen exchange kinetics in proton-conducting ceramic fuel cells: Effect of electronic leakage current using symmetric cells. *J. Power Sources* **242**, 784–789 (2013).
- 45. Strandbakke, R. *et al.* Gd- and Pr-based double perovskite cobaltites as oxygen electrodes for proton ceramic fuel cells and electrolyser cells. *Solid State Ionics* **278**, 120–132 (2015).
- 46. Loureiro, F. J. A. *et al.* La4Ni3O10±δ BaCe0.9Y0.1O3-δ cathodes for proton ceramic fuel cells; short-circuiting analysis using BaCe0.9Y0.1O3-δ symmetric cells. *Int. J. Hydrogen Energy* **46**, 13594–13605 (2021).
- 47. Schichlein, H. *et al.* System Identification: A New Modelling Approach for SOFC Single Cells. in *Proceedings of The Electrochemical Society* vols 1999–19 1069–1077 (1999).
- 48. Ramos, T., Thydén, K. & Mogensen, M. Electrochemical Characterisation of Ni/(Sc)YSZ Electrodes T. Ramos. in *ECS Transactions* vol. 28 123–139 (2010).
- 49. Saccoccio, M., Wan, T. H., Chen, C. & Ciucci, F. Optimal regularization in distribution of relaxation times applied to electrochemical impedance spectroscopy: Ridge and Lasso regression methods - A theoretical and experimental Study. *Electrochim. Acta* 147, 470– 482 (2014).
- 50. Boukamp, B. A. & Rolle, A. Analysis and Application of Distribution of Relaxation Times in Solid State Ionics. *Solid State Ionics* **302**, 12–18 (2017).
- 51. Ivers-Tiffée, E. & Weber, A. Evaluation of electrochemical impedance spectra by the

- distribution of relaxation times. J. Ceram. Soc. Japan 125, 193–201 (2017).
- 52. Boukamp, B. A. & Rolle, A. Use of a distribution function of relaxation times (DFRT) in impedance analysis of SOFC electrodes. *Solid State Ionics* **314**, 103–111 (2018).
- 53. Hong, J., Bhardwaj, A., Bae, H., Kim, I. & Song, S.-J. Electrochemical Impedance Analysis of SOFC with Transmission Line Model Using Distribution of Relaxation Times (DRT). J. Electrochem. Soc. 167, 114504–114504 (2020).
- 54. Zare, A., Salari, H., Babaei, A., Abdoli, H. & Aslannejad, H. Electrochemical evaluation of Sr2Fe1.5Mo0.5O6-δ/Ce0.9Gd0.1O1.95 cathode of SOFCs by EIS and DRT analysis. *J. Electroanal. Chem.* **936**, 1–8 (2023).
- 55. Sasaki, J., Mizusaki, J., Yamauchi, S. & Fueki, K. Studies on Electrode Processes of Stabilized Zirconia Cell System by Complex Impedance Method. *Bulletin of the Chemical Society of Japan* vol. 54 1688–1692 at (1981).
- 56. Uchida, H., Tanaka, S. & Iwahara, H. Polarization at Pt electrodes of a fuel cell with a high temperature-type proton conductive solid electrolyte. *J. Appl. Electrochem.* **15**, 93–97 (1985).
- 57. Li, N. et al. Characterization of GdBaCo2O5+δ cathode for IT-SOFCs. J. Alloys Compd.
  454, 274–279 (2008).
- 58. Peng, R., Wu, T., Liu, W., Liu, X. & Meng, G. Cathode processes and materials for solid oxide fuel cells with proton conductors as electrolytes. *J. Mater. Chem.* **20**, 6218–6225 (2010).
- 59. Zhang, C. & Zhao, H. A novel cobalt-free cathode material for proton-conducting solid

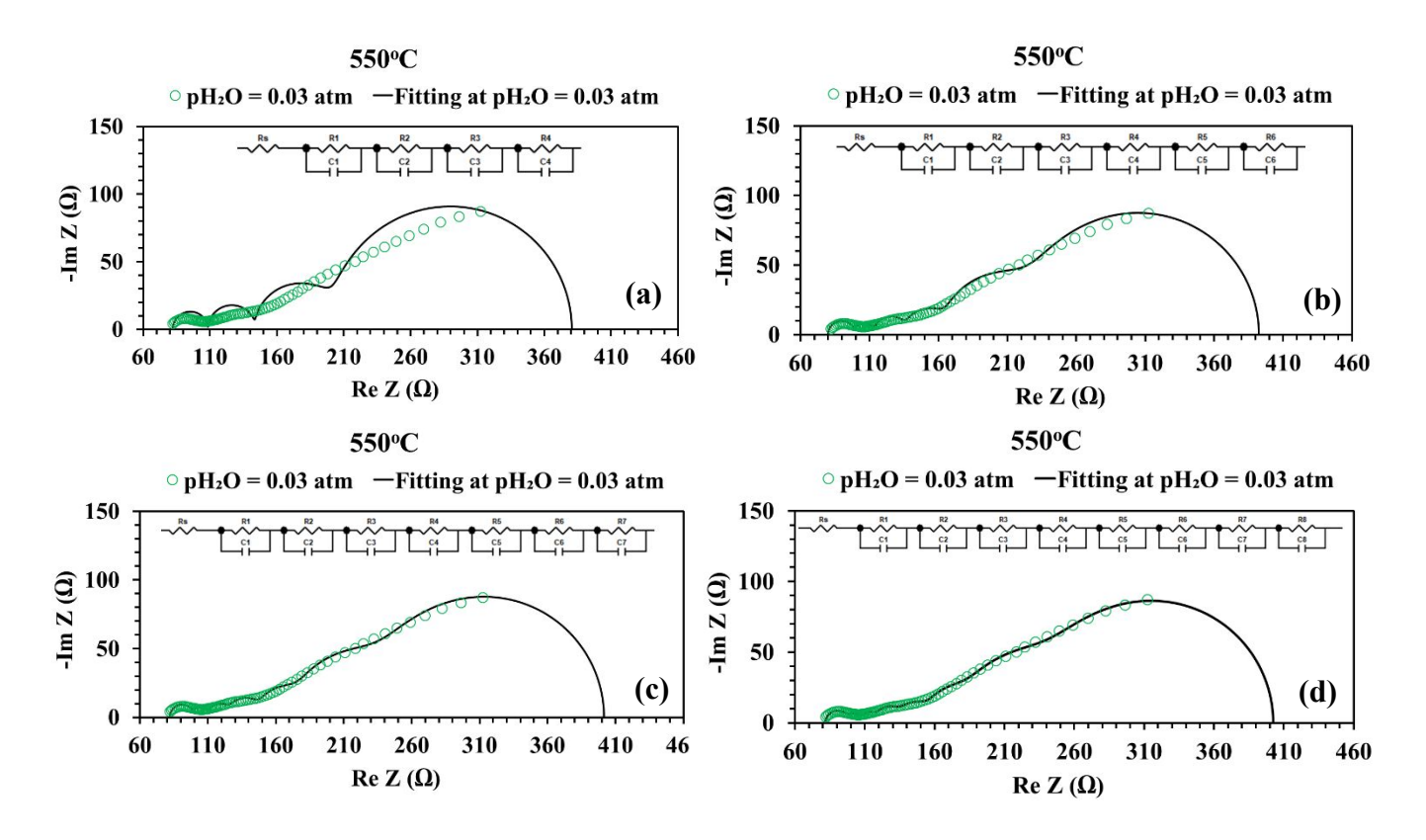
- oxide fuel cells. J. Mater. Chem. 22, 18387-18394 (2012).
- 60. Wang, Z. *et al.* A high performance cathode for proton conducting solid oxide fuel cells. *J. Mater. Chem. A* 3, 8405–8412 (2015).
- Radhakrishnan, R., Virkar, A. V. & Singhal, S. C. Estimation of Charge-Transfer
   Resistivity of Pt Cathode on YSZ Electrolyte Using Patterned Electrodes. *J. Electrochem.* Soc. 152, A927–A936 (2005).
- 62. Liu, M. & Hu, H. Effect of Interfacial Resistance on Determination of Transport Properties of Mixed-Conducting Electrolytes. *J. Electrochem. Soc.* 143, L109–L112 (1996).

# **Supplementary Materials for**

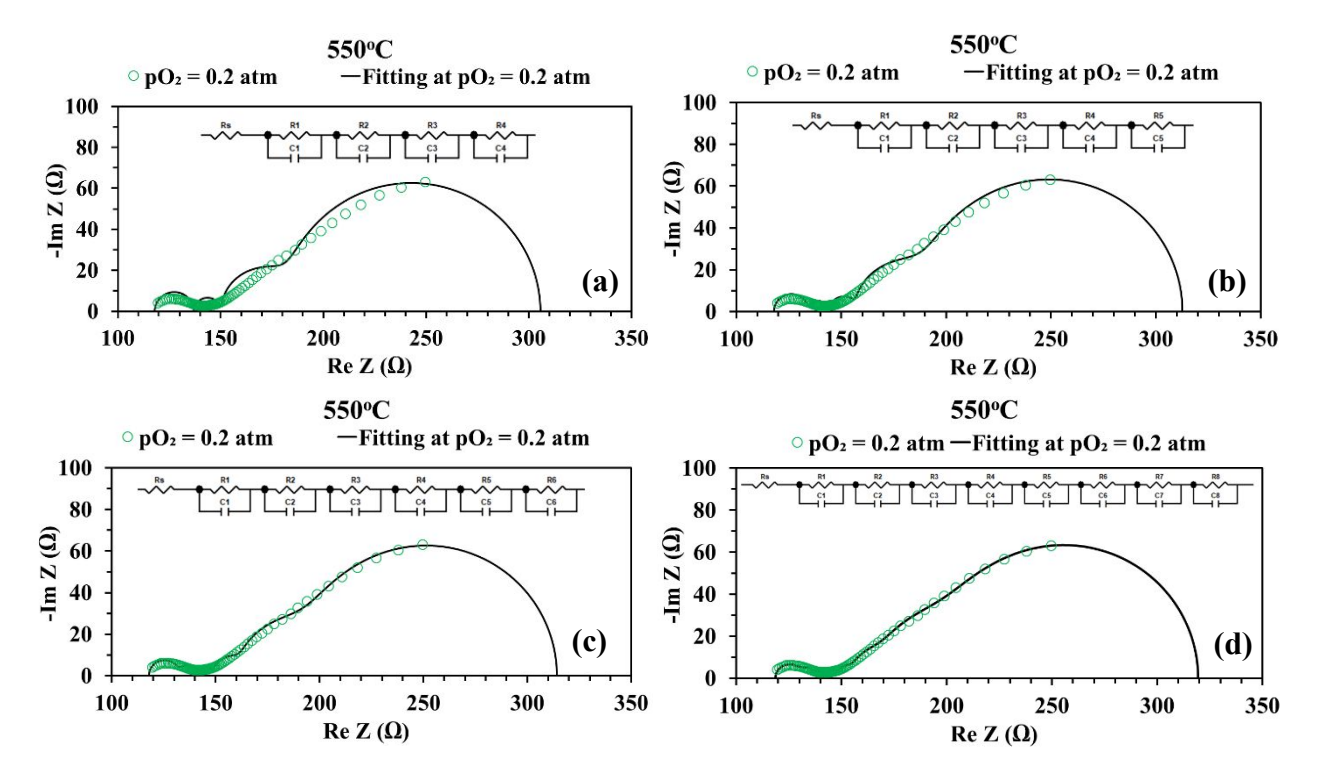
# Fabrication and Preliminary Testing of Silver Patterned Cathodes for Proton Conducting IT-SOFC

Md Shariful Islam Sozal, Wenhao Li, Suprabha Das, Borzooye Jafarizadeh, Azmal Huda Chowdhury, Chunlei Wang, Zhe Cheng\*

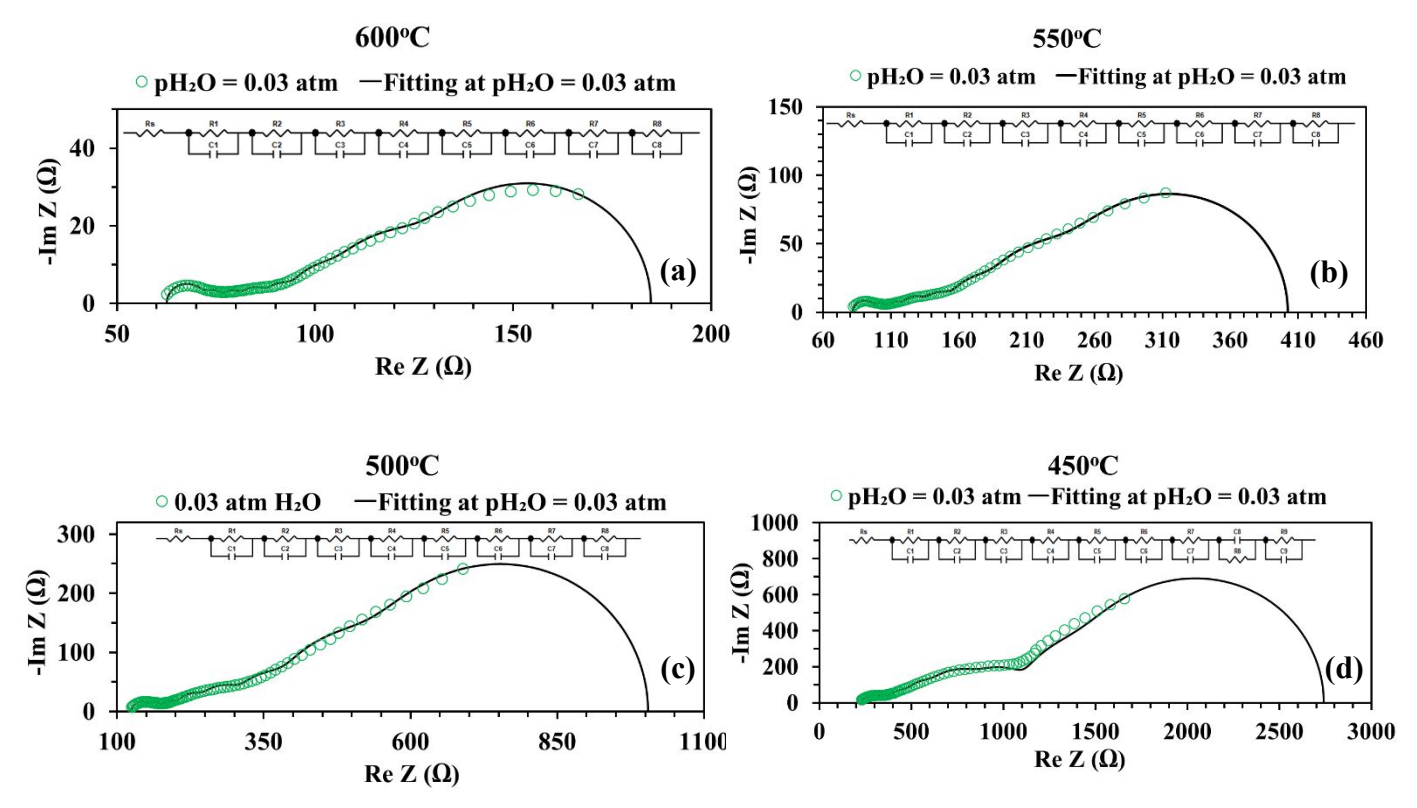
\*Correspondence: Dr. Zhe Cheng zhcheng@fiu.edu



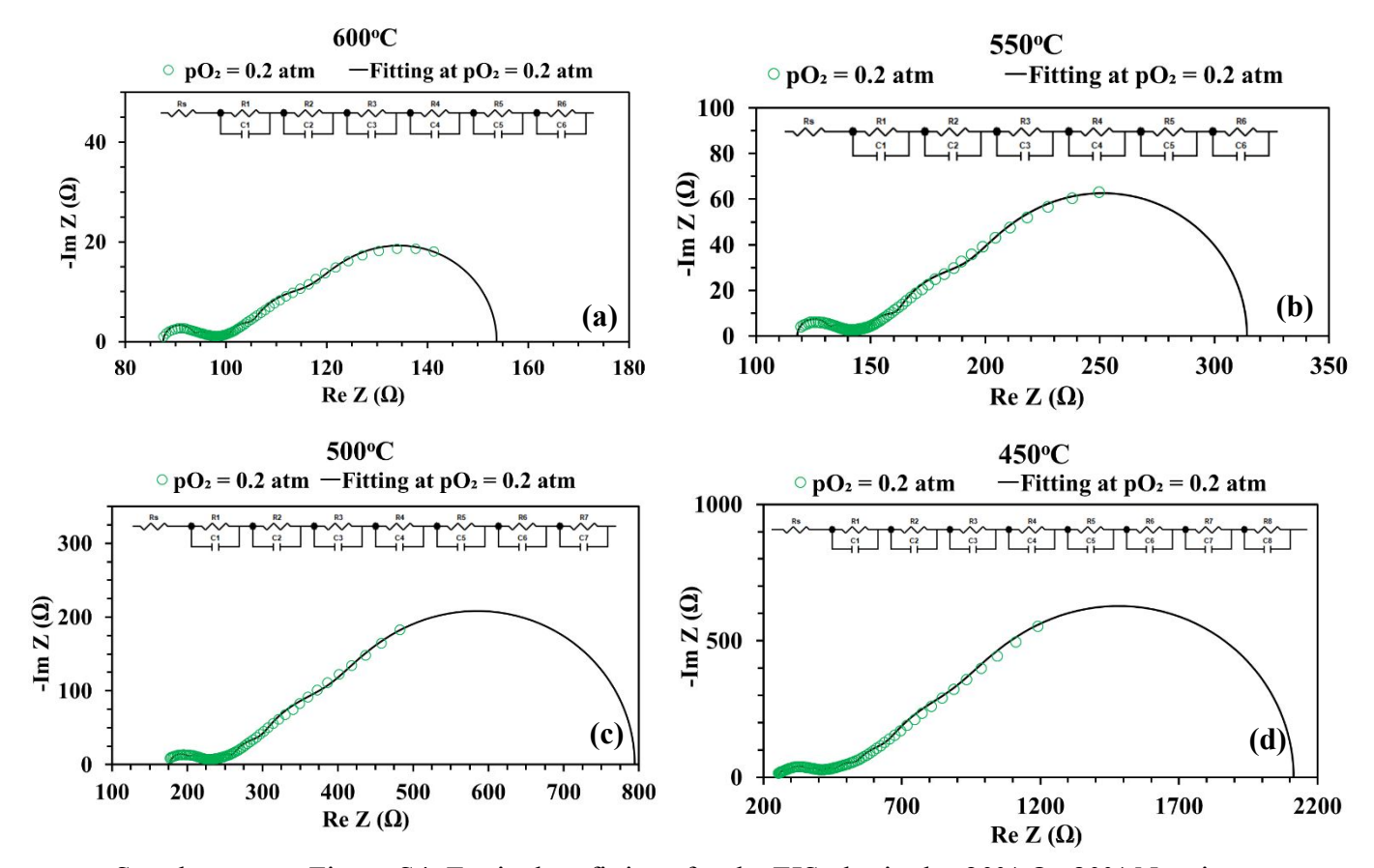
Supplementary Figure S1: Equivalent fittings for the EIS plot at 550 °C in simulated air with water addition at  $pH_2O = 0.03$  atm., considering (a) 4, (b) 6, (c) 7, and (d) 8 RC circuits.



Supplementary Figure S2: Equivalent fittings for the EIS plot at 550°C in dry 20%  $O_2$ -80%  $N_2$  mixture (i.e.,  $pO_2 = 0.2$  atm.), considering (a) 4, (b) 5, (c) 6, and (d) 8 RC circuits.



Supplementary Figure S3: Equivalent fittings for the EIS plot in simulated air with water addition at  $pH_2O = 0.03$  atm. at (a) 600, (b) 550, (c) 500, and (d) 450°C.



Supplementary Figure S4: Equivalent fittings for the EIS plot in dry 20%  $O_2$ -80%  $N_2$  mixture (i.e.,  $pO_2 = 0.2$  atm.) at (a) 600, (b) 550, (c) 500, and (d) 450°C.